1. INTRODUCTION

The Pebble bed modular reactor (PBMR) is a helium-cooled, graphite-moderated high temperature reactor (HTR). The PBMR will consist of a vertical steel reactor pressure vessel with a 6.2 m inner diameter and about 27 m high. To remove the heat generated by the nuclear reaction, helium coolant enters the reactor vessel at a temperature of about 500°C and at a pressure of 9 MPa. It then flows down between the hot fuel spheres, after which it leaves the bottom of the vessel, having been heated to a temperature of about 900 °C. The heated gas directly drives a power -turbine-compressor mounted on a single shaft. This shaft is coupled to a generator through a speed reduction gearbox. The coolant exits the power turbine at about 500°C and at a pressure of about 3 MPa. It then passes through a high efficiency recuperator. After the recuperator the gas is cooled and recompressed in two stages after which it returns to the reactor core after being reheated to 500°C in the secondary side of the recuperator[1].

PBMR fuel is based on a proven, high-quality German fuel design consisting of low enriched uranium triple-coated isotropic (LEU -TRISO) particles contained in a moulded graphite sphere[1]. A coated particle comprises of a kernel of uranium dioxide surrounded by four coating layers: the porous carbon layer, inner pyrolytic carbon layer, silicon carbide layer and the outer pyrolytic carbon layer (which form the so-called tri-structural isotropic particle (TRISO))[2]. In the coated particle fabrication process, a solution of uranyl nitrate is sprayed to form micro-spheres, which are then gelled and calcined to produce uranium dioxide fuel “kernels”. The kernels are then run through a chemical vapour deposition (CVD) furnace (typically using a gaseous environment at a temperature of 1 000 ºC) in which layers of specific composition can be added with extreme precision[3].

This study aims to compare experimental SiC TRISO particles from different batches that were produced under various conditions in the CVD coater. This serves the purpose of comparing the experimental PBMR particles with others known to have superior properties. All batches were produced by PBMR. The kernels used are ZrO_2 and not radioactive UO_2. This comparison is done by making use of different analytical methods, each with its own strengths and limitations.

The SiC layer plays a key role in the TRISO particle coating layer because it provides mechanical strength for the particle and acts as a barrier to diffusion of metallic and gaseous fission products. Since there are in excess of 200 SiC polytypes to date[4], the characterization of SiC polytypes is particularly challenging. However it has been shown that the most commonly occurring polytypes of SiC (namely 3C, 2H, 4H, 6H, 8H and 15R) can be characterized by Raman spectroscopy[5] and the Rietveld method of X-ray diffraction[6]. The most definitive means of SiC polytype characterization however is with transmission electron microscopy and selected area electron diffraction. There are however few studies that focus specifically on the SiC layer of TRISO particles.

From communication with PBMR, it has been established that the SiC prepared by chemical vapour deposition has the following general properties[7]:

- As the main retention layer the SiC is rather brittle in tension but strong in compression
- Methyl trichlorosilane (MTS) is used in coating SiC, where Si and C combine in a 1:1 ratio at an optimum temperature of about 1550°C. A lower temperature leads to a greater proportion of free silicon, while a higher temperature leads to a greater proportion of free carbon
- The size of SiC crystals may play a significant role in the effectiveness of the layer as a barrier

2. LITERATURE REVIEW

2.1. TRISO particle properties

The Tri-structural isotropic (TRISO) coated fuel particles consist of a micro-spherical kernel of uranium oxide or oxycarbide fuel and coating layers. These consist of a porous pyrolytic carbon (PyC) layer, the inner PyC (IPyC) layer, the silicon carbide (SiC) layer, and outer PyC (OPyC) layer. Figure 2.1 illustrates these layers schematically. The function of the coating layers is to retain fission products within the particle[8]. The TRISO layer also functions to withstand the thermo-mechanical stresses generated during burnup[9].

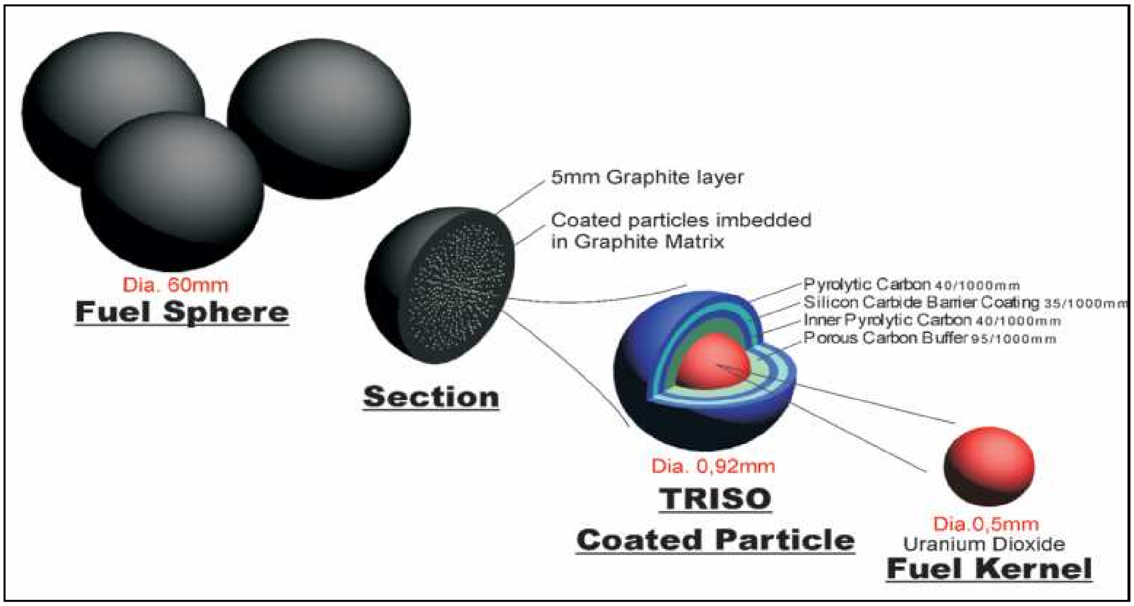

Figure 2.1 – Schematic diagram of TRISO particles and the respective layer thicknesses[10].

The low density porous PyC coating layer is called the buffer layer (about 50% void) and attenuates fission recoils and provides void volume for gaseous fission products including carbon monoxide. It also accommodates kernel swelling without transmitting forces to the outer coatings. The high density, isotropic IPyC coating layer contains the fission products and carbon monoxide during irradiation, protects the kernel from reactions with chlorine during SiC deposition and provides structural support for the SiC layer. The SiC coating layer provides the mechanical strength to withstand stresses developed due to irradiation-induced dimensional changes in the pyrolytic carbon layer. Secondly, it acts as a barrier to high pressure diffusion of gaseous and metallic fission products generated in the kernel/buffer region, which diffuse easily through the IPyC layer. The function of the high density OPyC layer is to protect the SiC during the remainder of the fabrication process and to provide structural stability to the SiC coating during irradiation[8,11].

The coating layers should ideally be intact before and during irradiation. It is the case in practice that a small fraction of the particles with defective coatings are present in the fabrication batch. A defective SiC layer carries the greatest risk from the point of view of fission product retention. The burn leach test is used to detect defective SiC layers. In this test, particles are heated to 800 to 900°C in air in order to oxidize the OPyC layers. Acid leaching of the exposed uranium follows. The defective SiC layer of coating will then expose uranium upon burning[12].

2.2. Silicon carbide – basic background

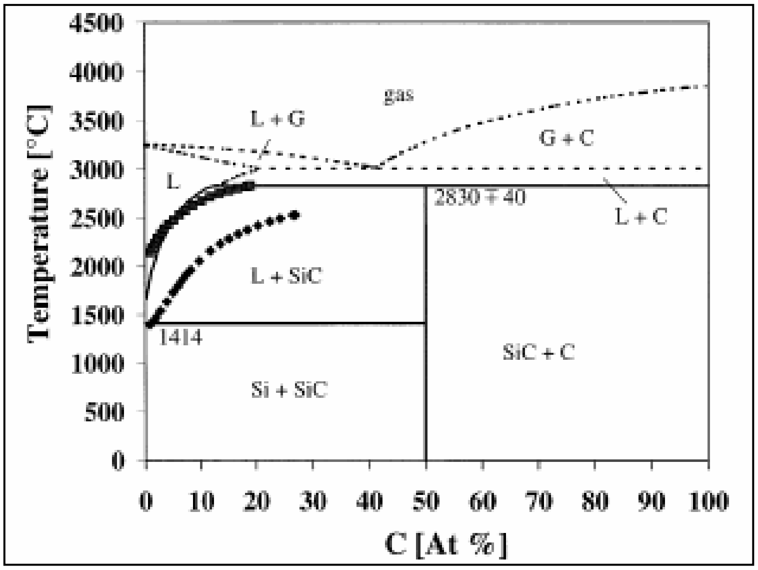

Figure 2.2 – The Si-C binary phase diagram system at $p \leq 1$ bar[13]. The dotted line[14], square[15] and diamond[16] scatter points all show data available from literature.

Silicon carbide is the only solid phase binary compound of silicon and carbon under standard conditions. This is confirmed by figure 2.2, which is a binary phase diagram of silicon and carbon. It is evident that the solubility (X) of C in liquid Si is low, reaching a maximum value of X ~15 mol% (at 2830°C). The solubility ranges from 0.5 to 7 mol% between 1800 and 2300°C [13].

SiC has a very high thermal stability. It is not possible to melt it at atmospheric pressure as it sublimes and dissociates into C and Si-rich vapour. Dissociation and sublimation are appreciable above 2000°C[14]. From pressure experiments the peritectic reaction occurs at 2830 (±40°C)[15]. Under such the solid decomposes into a Si-rich liquid in graphite. As a result silicon carbide has no congruent melting point[17].

It has been reported that the coating temperature is the main variable affecting the content of free silicon and density. At temperature below 1400°C - 1500°C, the free silicon was found to increase with decreasing coating temperature. The density was found to decrease with increasing free silicon content[18].

Silicon carbide is one of the hardest materials, with a Moh's scale hardness of 9 (between diamond (10) and topaz (8)). It also has a high resistance to wear with a value of 9.15 when compared with diamond at 10.00 and corundum at 9.00[19]. The SiC prepared by chemical vapour deposition (CVD) has good mechanical properties and good stability against oxidation[18] . CVD SiC is synthesized using MTS (Methyl Tri-Chlorosilane) according to equation 2.1:

$$CH_3SiCl_3 \rightarrow SiC + 3HCl \qquad (2.1)$$

2.3. Polytypism of SiC

The ability of compounds and elements to occur in more than one crystal structure is termed polymorphism. The one-dimensional variation of this is polytypism. Polytypes differ by the stacking sequence along one direction[17]. Polytypism refers to the occurrence of different stacking sequences in the same material and can reflect a change of physical properties with a change in crystal structure[4]. The physical properties that are observed are strongly dependent on the amounts of the various polytypes[20].

There are in excess of 200 SiC polytypes (one cubic (C), and numerous hexagonal (H) and rhombohedral (R) ones). Of these the most common polytypes are 3C, 4H, 6H and 15R[11]. Silicon carbide exhibits an extensive range of well ordered structures[4,21]. The rhombohedral and hexagonal classes of SiC polytypes are collectively called α-SiC and the cubic class (consisting of one member) is called β-SiC[22].

Polytypes of SiC arise from different periodic stacking sequences of bilayers[23]. This is seen from figure 2.3. There are six different bilayers each consisting of two close packed planes of polytypes described by different stacking sequences of Si-C double layers, perpendicular to the close-packed plane; i.e. [111] for cubic and [0001] for hexagonal[4]. The stacking sequences of the atomic double atomic planes Si-C along the c-direction are different and the polytypes are regarded as natural superlattices[5]. Bilayers stack to form vertex-sharing tetrahedral cages of Si_4C (or SiC_4) with a C (or Si) atom at the center of each cage. The stacking sequence does not significantly alter bond lengths or affect bulk density (3.2 g/cm^3) [24]. With a Si-C bond distance $\delta = 1.89$ Å, bilayers are spaced $4/3\ \delta \approx 2.52$ Å apart. If the number of bilayers in the unit cell is even, the symmetry must be hexagonal; otherwise it is cubic or rhombohedral[4].

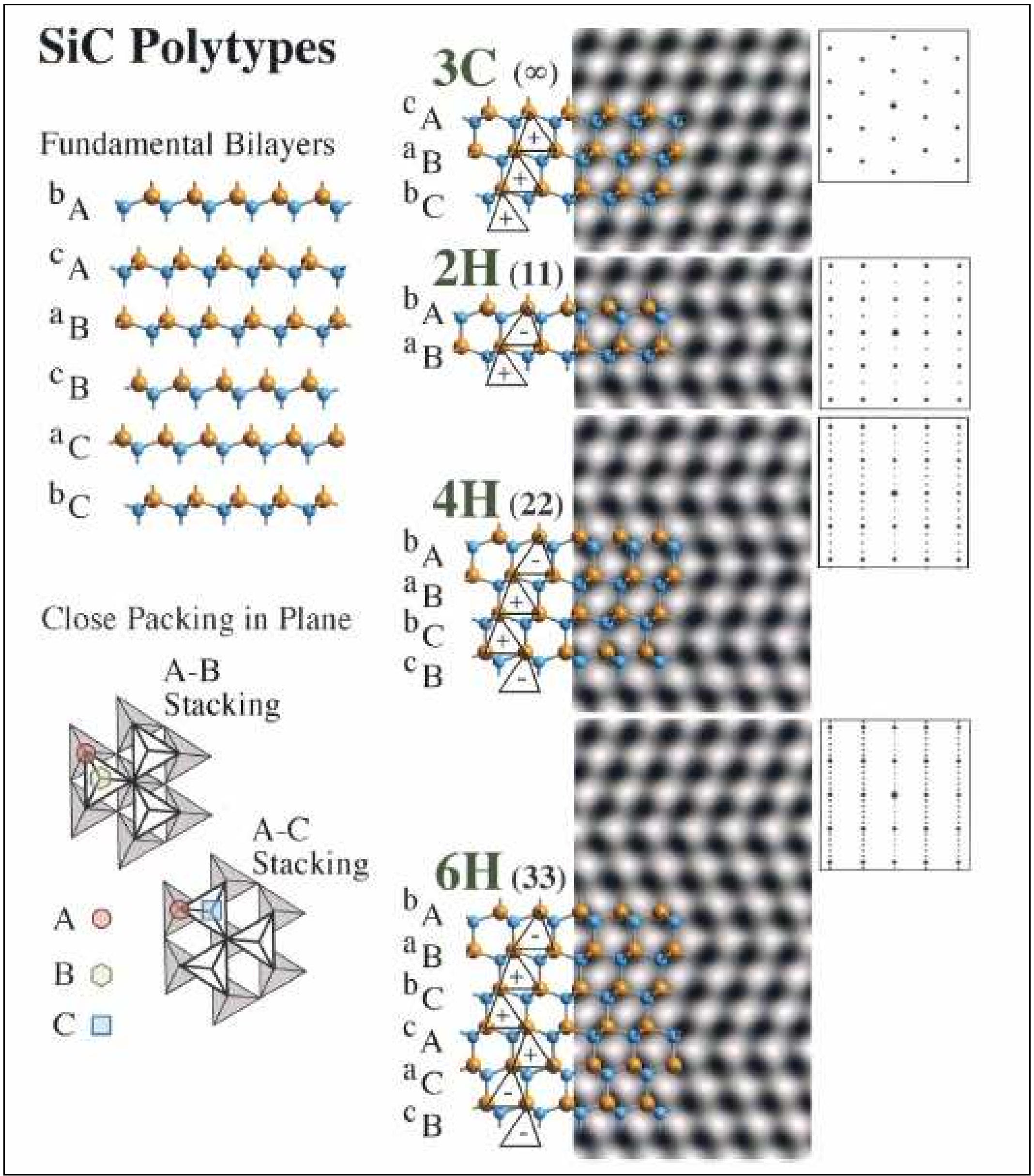

Figure 2.3 – Silicon carbide polytype structures[23]. Polytypes of SiC are formed by periodic stacking sequences of bilayers that produce tetrahedral sheets. Atomic models of the six unique (fundamental) bilayers (*bA*, *cA*, *aB*, *cB*, *aC*, and *bC)* of SiC (top left) based on three principal close packed planes (*A*, *B*, and *C*) (lower left) are shown. Blue atoms represent C and orange atoms represent Si. The two basic stacking arrangements, *A-B* and *A-C* that form planes of vertex-sharing parallel and antiparallel tetrahedra, respectively, are shown (lower left). Atomic models of the four simplest, 3C/(∞), 2H/(11), 4H/(22), and 6H/(33), polytypes are shown superimposed on calculated HR-TEM lattice images produced using defocus conditions that reproduce the symmetry of the projected lattice

(center column). Schematic illustrations of diffraction patterns (including forbidden reflections in some cases) are also shown (right column).

A number of notation schemes are used to describe SiC polytypes. The Ramsdell[25] notation is such that a polytype is denoted by the number of bilayers in the unit cell followed by C, H, or R, denoting the crystal symmetry (i.e., cubic, hexagonal, or rhombohedral). The fundamental bilayers are denoted *bA*, *cA*, *aB*, *cB*, *aC*, and *bC*. In the earlier Zhdanov[26] notation, sheet tetrahedra are assigned a positive or negative sense defined by a relative rotation of radians about the stacking direction (as is shown in figure 2.3). The successive number of tetrahedral layers, having tetrahedra with a common positive or negative sense, is counted in each subseries present. For example, the polytype denoted 6H (i.e. {. . .*AaBbCcAaCcBb*. . .}) in the Ramsdell notation (figure 2.3) has two subseries each consisting of three tetrahedral layers of the same sense, {. . . +++ ---. . .}, and in the Zhdanov notation is denoted (33). The polytype denoted 3C (i.e., {. . .*AaBbCc*. . .}) in the Ramsdell notation has an infinite number of tetrahedral layers of the same sense in one subseries, {. . .+. . .}, and is denoted (∞) (figure 2.3)[23].

2.3.1. Cubic 3C/(∞), β-SiC polytype

The cubic SiC polytype has the second smallest unit cell, with a $F\bar{4}3m$ space group (unit cell length a = 4.36 Å). This structure is formed by the stacking sequence {. . .*AaBbCc*. . .} of three bilayers, and is denoted 3C in the Ramsdell notation and (∞) in the Zhdanov notation. Cubic 3C-SiC is iso-structural to cubic 3C diamond and consists of two interpenetrating face-centered cubic (FCC) sublattices, one lattice entirely Si and one entirely C, which are separated by the displacement vector a/4 [111]. Tetrahedra lie in (111) planes and the 3C stacking sequence of tetrahedral planes is best viewed along the [011] zone axis[23].

2.3.2. Hexagonal 2H/(11), α-SiC polytype

This polytype has the smallest unit cell (lowest order) and is hexagonal (space group *P*63*mc*, unit cell lengths a = 3.08 Å, c = 5.03 Å). This structure is formed by the stacking sequence {. . .*AaBb*. . .}, and is denoted 2H in the Ramsdell notation and (11) in the Zhdanov notation. Hexagonal 2H α-SiC is iso-structural to hexagonal 2H diamond (lonsdaleite). It is the only polytype with a 1 in its Zhdanov symbol; meaning that no other polytype contains subsequences of 2H order. Tetrahedra lie in {0001} planes and the 2H stacking sequence of tetrahedral planes is best viewed along the $[11\bar{2}0]$ zone axes[23].

2.3.3. Higher order α -SiC polytypes (unit cells larger than 3C)

Lattice images of α-SiC along zone axes perpendicular to the tetrahedral stacking direction and analogous to 3C $[01\bar{1}]$ and 2H $[11\bar{2}0]$ display a characteristic zigzag contrast pattern reflecting their Zhdanov symbol, under defocus conditions where the symmetry of the open channels in the structure is reproduced. Furthermore, the different polytypes can be readily identified by their electron diffraction patterns and HR-TEM images[23].

2.3.4. Factors influencing polytypism

Polytypic structure is influenced by dopants. By increasing the partial pressure of nitrogen (n-type dopant), the formation or growth of 3C-SiC is promoted. Aluminium (p-type dopant) increases the probability if 6H or 4H formation. In the case of 3C-SiC, SiC growth occurs at temperatures of up to 2475K, in the presence of supersaturated Si vapour. This sometimes leads to the formation of a silicon liquid phase. Solid-state phase transformation between SiC polytypes has been illustrated in the literature as a function of temperature and applied stress[4]. If a solid phase has several modifications, one is usually the thermodynamically stable one while the others are metastable. Formation of one or more metastable phases is often observed. Most theories that explain the formation of certain polytypes are usually based on the following[4]:

- Impurities
- Si/C ratio
- Temperature
- Presence of dislocations
- Presence of vacancies ordered in superlattices
- Stacking fault energy
- Formation of polymers within the gas phase
- Non-equilibrium conditions within the vapour phases
- Surface vibrational entropy contribution to free energy
- Native defects
- Surface superstructures

2.4. Raman theory

2.4.1. The Raman effect

Raman scattering or the Raman effect is the inelastic scattering of a photon. When light is scattered from an atom or molecule, most photons are elastically scattered (Rayleigh scattering). The scattered photons have the same energy (frequency) and wavelength as the incident photons. However, a small fraction of the scattered light (approximately 1 in 1 million photons) is scattered by an excitation, with the scattered photons having a frequency different from, and usually lower than, the frequency of the incident photons[27].

Scattering is defined as light deflected from the original direction of propagation of the incident light. From spectral analysis of the light scattered there exist discrete components of altered wavenumbers in addition to Rayleigh scattering (scattering of light without change in the wavenumber of the incident light). There are in general, pairs of new lines appearing in the spectrum at wavenumbers positioned symmetrically relative to the Rayleigh line[28,29,30]. Figure 2.4 shows the possibilities that occur when radiation is scattered. Molecules in the ground state give rise to Raman scattering with energy $h(\nu_0 - \nu_1)$. Molecules in a vibrationally excited state scatter inelastically back to the ground state, giving the Raman-effect with an energy of $h(\nu_0 + \nu_1)$.

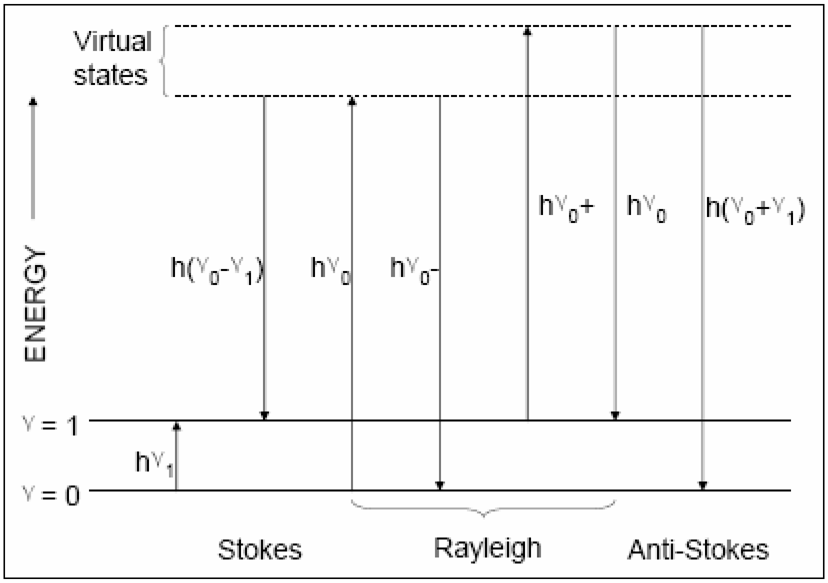

Figure 2.4 – Energy level diagram, illustrating the fundamental processes of Raman scattering, adapted from Grasselli et al, (1981) [28]

The appearance of altered frequencies (wavenumbers) in scattered light is called the Raman effect or Raman scattering. The Rayleigh scattering that accompanies Raman scattering is usually 3-5 orders of magnitude greater, rendering the latter a feeble effect. The Rayleigh scattering itself is 3-4 orders of magnitude lower than the intensity of the incident exciting radiation. The new components that appear in the spectrum of the scattered radiation at shifted wavenumbers are called Raman lines or Raman bands and collectively they are referred to as the Raman spectrum. The Raman bands at wavenumbers less than the exciting wavenumber $(\nu_0 - \nu_1)$ are the Stokes lines, while those that appear at higher wavenumbers are anti-Stokes lines $(\nu_0 + \nu_1)$. Generally, the anti-Stokes lines are considerably weaker and quickly diminishing in intensity with increasing ν_1 relative to the Stokes lines[31]. Frequency shifts of Stokes and anti-Stokes Raman spectra correspond to the frequency of the normal modes of molecular vibrations. The shift values are therefore more valuable for characterizing band position, rather than the absolute wavenumbers. Most Raman applications use the more observable Stokes side of the Raman spectrum and the plot is on a relative scale ($\nu_0 - \nu = \nu_1$)[28].

Dispersive Raman spectroscopy uses a visible laser for excitation, a dispersive spectrometer and a charge coupled device (CCD) for detection. The main disadvantage of using visible excitation is common to all visible spectrometer systems and this is fluorescence. Since Raman scattering is a weak effect, a powerful excitation source is chosen to provide a high power density at the sample. The implication is that fluorescence can not only occur from the sample under investigation, but also from any contaminant which is fluorescent. Fluorescence will not occur at energies below that of excitation and it can therefore be intense in the energy region covered by Stokes Raman scattering. As a result, interference often occurs and accounts for why Raman scattering is not more widely used[29].

2.4.2. Theoretical overview

The classical description of Raman scattering is of a polarization induced in the molecule by the oscillating electric field of the incoming light. The induced dipole then radiates scattered light with or without exchanging energy with vibrations in the molecule. The effect is described by the equation 2.2 below and describes the case for both classical and quantum mechanical treatments of Raman scattering[30]:

$$P = \alpha E \qquad (2.2)$$

Where: P is the strength of the induced dipole
α refers to the molecular polarizability
E is the incident electric field

The classical treatment of Raman scattering is based on the effects of molecular vibrations on the polarizability α. The electric field resulting from the incident radiation is a time-varying function as is shown by equation 2.3.

$$E = E_0 \cos 2\pi v_0 t \tag{2.3}$$

Where: v_0 is the frequency of the laser light

The molecular vibrations are usually composed of normal modes, Q_j, where there are 3N-6 (and 3N-5 for a linear molecule) modes for a molecule of N atoms.

$$Q_j = Q_j^o \cos(2\pi \ v_j \ t) \tag{2.4}$$

Where: v_j is the characteristic harmonic frequency of the j-th normal mode.

Q_j is the j-th normal coordinate of the vibration

When a molecule vibrates, the polarizability is also a time-varying term which depends on the vibrational frequency of the molecule.

$$\alpha = \alpha_0 + \left(\frac{\delta\alpha}{\delta \ Q} \right) Q_j + \ldots \tag{2.5}$$

The polarizability of electrons in the molecule is modulated by the molecular vibration as is shown in figure 2.5. A combination of equations 2.2, 2.3 and 2.5 yields equation 2.6; assuming that the higher order terms of equation 2.5 are ignored. Raman scattering occurs because a molecule can change the polarizability. The change is described by the polarizability derivative $\frac{\delta\alpha}{\delta Q_j}$.

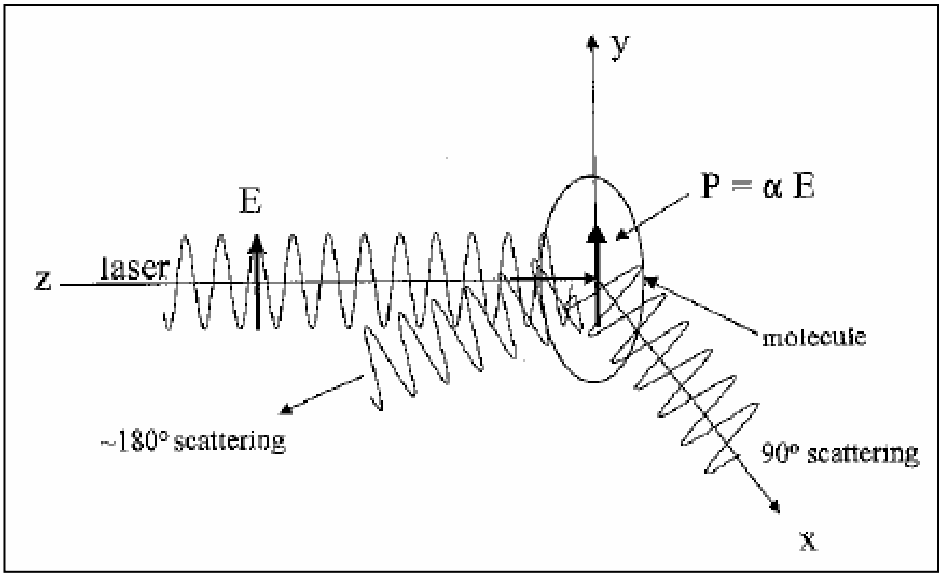

Figure 2.5 – Polarization (P) induced in a molecule's electron cloud induced by an optic electric field E, shown for 90° and 180° geometry[30].

$$P = \alpha_0 E_0 \cos(2\pi\ v_j\ t) + E_0 Q_j^o \left(\frac{\delta\alpha}{\delta\ Q}\right) \frac{\cos 2\pi(v_0 + v_j)t + \cos 2\pi(v_0 - v_j)t}{2} \tag{2.6}$$

When polarized electrons radiate light at the frequency of their oscillations, scattering occurs at three frequencies, as is confirmed by equation 2.6. The first term denotes Rayleigh scattering, which is the same frequency as the laser. Its magnitude is proportional to α_0 which is the inherent polarizability of the molecule. The second term is the anti-Stokes Raman scattering and occurs at $(v_0 + v_j)$. The third term is the Stokes Raman scattering at $(v_0 - v_j)$.

Equation 2.6 is derived classically and is incomplete, with the following implications[30]:

- Polarization and scattering (Raman and Rayleigh) intensities are linear with the laser intensity. Even though non-linear Raman scattering can occur at high E_0 values, this is not an issue in analytical applications.
- Only vibrations that change the polarizability (hence the $\delta\alpha/\delta Q \neq 0$) yield Raman scattering. This governs the primary selection rule for Raman scattering.
- Raman shifts may be both positive and negative. The Raman anti-Stokes intensity depends on the population of the first vibrationally excited state, its intensity is related to temperature by the Boltzmann distribution, which is given by equation 2.7, for the case of non-degenerate vibration.
- $\delta\alpha/\delta Q_j$ may vary greatly for different molecules and different modes within a molecule, leading to a wide variation in Raman scattering intensity
- $\delta\alpha/\delta Q_j$ is generally much smaller than α_0 and Raman scattering is much weaker than Rayleigh scattering, even though this is not apparent from equation 2.6.

The observed intensity of Raman scattering is proportional to the cross-section σ_j (square centimeters per molecule). The magnitude of σ_j is related to $\delta\alpha/\delta Q_j$. The effect of this relationship is shown in equation 2.7, where the Raman intensity is shown to vary with frequency.

$$\frac{I_R(v_0+v_j)}{I_R(v_0-v_j)} = \frac{(v_0+v_j)^4}{(v_0-v_j)^4}\exp\left(\frac{-hv_j}{kT}\right) \qquad (2.7)$$

From equation 2.8, it is evident that the Raman intensity varies with the fourth power of the observed frequency for normal Raman scattering, which depends on the laser frequency. The v^4 factor gets derived from the classical treatment of scattering from an oscillating induced dipole. The scattered light occurs at an absolute frequency of $\bar{v}_0 \pm \bar{v}_j$.

$$I_R = \mu'(\bar{v}_0 \pm \bar{v}_j)^4 \alpha_j^2 Q_j^2 \qquad (2.8)$$

Where : I_R is the Raman intensity

μ' is a constant

$\bar{v}_j$ is the Raman shift (in reciprocal centimeters)

Raman Cross section

In addition to the factors affecting the Raman intensity, such as the laser wavelength and polarizability, the empirically determined cross-section is equally important for analytical applications. This is especially true in cases involving weak or characteristic scattering from several components. The polarization, laser wavelength and observation geometry are often invariant, being determined by the instrument. This makes it sufficient to use the empirical cross section for a given Raman band in that geometry to estimate the signal strength. The cross section, denoted as σ_j (centimeters squared per molecule) is proportional to the probability of an incident photon being scattered as a Raman-shifted photon with a particular Raman shift[30].

For the classic approach the Raman scattering (watts) is related to the cross-section and laser intensity (I_0 in watts) by equation 2.9.

$$I_R = I_0 \sigma_j D dz \tag{2.9}$$

Where : D is the number density of scatters (molecules per cubic centimeter)

dz is the path length of the laser in the sample

For a scatter that is not resonant or pre-resonant (which follows the classical $\bar{v}^{-4}$ dependence) a frequency independent cross-section σ_j^o (centimeters to the sixth power per molecule) may be defined by equation 2.10.

$$\sigma_j^o = \frac{\sigma_j}{(\bar{v}_0 - \bar{v}_j)^4} \tag{2.10}$$

Where: $\bar{v}_j$ is the vibrational frequency of the Raman mode (in cm^{-1})

$\bar{v}_0 - \bar{v}_j$ is the absolute frequency of scattered light (in cm^{-1})

$\bar{v}_0$ and $\bar{v}_j$ are expressed in wavenumbers (in cm^{-1})

The introduction of photon counting detectors into Raman instrumentation has meant that current spectrometers count photons as opposed to measuring watts, with the two differing by a factor of hv. Photons counting derivations are more consistent with a quantum mechanical treatment whereas the classical derivation is based on induced dipoles. Equation 2.11 is the result of equation 2.9 rewritten for photon counting systems.

$$P_R = P_0 \sigma_j^{'} Ddz \tag{2.11}$$

P_R and P_0 have units of photons per second, while $\sigma_j^{'}$ has a different frequency dependence than for equation 2.10. The substituting of σ_j from this equation into equations 2.9 and 2.11 yields equation 2.12.

$$I_R = I_0 \sigma_R^o (\bar{v}_0 - \bar{v}_j)^4 Ddz \tag{2.12}$$

Since $I_R = P_R hc(\bar{v}_0 - \bar{v}_j)$ and $I_0 = P_0 hc\bar{v}_0$ equation 2.12 can be rewritten as:

$$P_R = P_0 \sigma_j^o \bar{v}_0 (\bar{v}_0 - \bar{v}_j)^3 Ddz \tag{2.13}$$

and

$$\sigma_j^{'} = \sigma_j^o \bar{v}_0 (\bar{v}_0 - \bar{v}_j)^3 \tag{2.14}$$

Hence whenever P_R is measured in photons per second, the Raman intensity scales with $\bar{\nu}_0(\bar{\nu}_0 - \bar{\nu}_j)^3$ as opposed to $(\bar{\nu}_0 - \bar{\nu}_j)^4$.

The differential Raman cross-section is defined as $d\sigma_j / d\Omega$ where Ω represents the solid angle of collection (equation 2.15).

$$\beta(cm^2 molecule^{-1} sr^{-1}) = \frac{d\sigma_j}{d\Omega} \tag{2.15}$$

Equation 2.15 can be summarized as $\frac{d\sigma_j}{d\Omega} = \frac{\text{scattered flux / unit of solid angle}}{\text{incident flux / unit of surface}}$, where the units are $cm^2 molecule^{-1} sr^{-1}$. The sr^{-1} term refers to the reciprocal of the steradian (the SI unit of solid angle). The symbol β is used to differentiate from the integrated σ_j and from the cross section differentiated with respect to the observation angle and with respect to the wavelength β' (equation 2.16). β' depends both on observation direction and the Raman shift.

$$\beta'(cm^2 molecule^{-1} sr^{-1} wavenumber^{-1}) = \frac{\delta^2 \sigma_j}{\delta\Omega\,\delta(\Delta\bar{\nu})} \tag{2.16}$$

2.4.3. Raman Spectroscopy of condensed phases

The analysis of solids with Raman spectroscopy is significantly more complex than is the case with liquids and gases since atoms, ions or molecules may be distributed with either no long-range order (amorphous), perfect order in one, two or three dimensions (crystalline) or a mixed state (semi-crystalline). As is the case with infra-red spectroscopy, Raman spectroscopy is highly sensitive to the state of order in solids[32].

In a crystal, the vibration selection rules depend upon the symmetry and the occupancy of the unit cell and the molecular symmetry (molecules are classified according to symmetry elements or operations that leave at least one common point unchanged). Generally, when a molecule is placed at a lattice site of lower symmetry than its point group, the molecule is perturbed and more bands can appear due to removal of vibrational degeneracy (band splitting)[32]

Disordered solids

In extreme cases of disordered material such as inorganic glass or an amorphous polymer, translational periodicity is very low and a wide range of local molecular environments exist. This gives rise to very broad features in place of sharp bands observed from crystals[32].

Influence of sample form

The sample form can have a significantly large influence on Raman band intensities, shapes and positions. These factors are particularly significant when interpreting spectra to draw quantitative conclusions[32].

Size effects in polycrystalline particles – diffuse reflection

The overall scattering intensity can be strongly dependent on the particle size and particle packing. This happens because both the laser beam and the Raman radiation will suffer multiple elastic scattering events in a polycrystalline powder. The observed Raman intensity will then depend on the diffuse reflectivity of the sample. The effect of forward and backscattered Raman intensities have been related to the incident laser power, sample thickness, sample absorption, elastic scattering coefficient and the Raman scattering coefficient by means of the Kubelka-Munk theory[33]. The basic results are that[32]:

- The Raman intensity decreases as the particles get smaller
- For samples with a low absorption coefficient, the Raman/Rayleigh ratio is maximized by using coarse powders in a forward scattering arrangement

- For strong absorbers it is better to use coarse powders and backscattering geometry

Absolute Raman intensities from powders are of limited use because they will be influenced by particle size. The use of a powder standard as an intensity standard is therefore not recommended. Quantitative measurements of heterogeneous powders should be made using band ratio methods. This will necessitate the measuring of two or more compounds by ratioing discrete Raman bands that arise from each of the compounds. This approach could be invalid if the particle sizes of the components vary from sample to sample. The particle sizes in a calibration need to be similar to those of the sample; otherwise the intrinsic Raman intensity of each component will not be constant. As the particle size drops significantly below 1 μm it is generally observed that the intrinsic scattering efficiency falls dramatically for non-surface modes. For instance, a 10 μm particle will have a much stronger intrinsic Raman spectrum than 0.01 μm particles of the same material[32].

The following artefacts can arise when dealing with condensed phases[32]:

Self absorption (colour)

If the sample possesses strong absorption bands in the absolute wavelength region of the Raman scatterer, the Raman scattered radiation will be attenuated. In some cases, the effect is obvious and expected – as such strongly coloured samples are likely to absorb Raman scatter excited by a visible laser. The absorption band of coloured samples is generally broad leaving a large region of the Raman spectrum suppressed. It has been shown through studies how attenuation can be quantified as a function of absorber concentration and optical properties[34]. The same study also showed that for a sample that absorbs both laser and Raman wavelengths, 180° backscattering is greatly preferred if the absorber molecule is also the Raman scatterer of interest. If 90° scattering is employed, it becomes necessary to carefully optimize the absorber concentration thereby maximizing its Raman signal, whereas 180° scattering efficiency reaches a plateau once the absorber reaches a sufficient concentration. In this case, the laser beam will penetrate deeply into the sample, yielding an analysis specific to the sample surface. In this case, it is best to use the widest aperture collection lens available in order to obtain the highest Raman signal.

Heating, degradation and fluorescence

Condensed samples are prone to heating in the laser beam, even if they are slightly coloured. This leads to subtle phase changes such as crystal form or conformational modifications. In addition the laser-induced heating can induce subtle, reversible effects such as band broadening and shifting as is the case with carbon[35]. These changes can be hard to avoid because the intensity at the laser focus can be very high, especially in Raman microscopy measurements. Therefore, even with a solid that does not visibly melt, burn or otherwise indicate damage, it is not safe to assume that the laser has not modified the sample. Where possible, spectra should be recorded using different laser powers to check for changes.

If the laser light is absorbed by the sample, this often leads to relatively intense fluorescence, which can severely degrade the signal-to-noise ratio of the Raman spectrum. Fluorescence can be minimized using a number of techniques to either clean up the sample chemically (removing the fluorescor) or to suppress the fluorescence signal by distinguishing Raman and fluorescence signals. However, the most effective universal approach is to shift the excitation laser to a longer wavelength (about 785 nm or 1064 nm) to avoid exciting electronic transitions.

2.4.4. Quantitative Raman spectroscopy

Both currently and historically, the majority of applications of Raman spectroscopy have been qualitative, with the objective being to determine the peak frequencies and comparing vibrational features to spectra from different laboratories, or those predicted theoretically. The vast majority of reported Raman spectra are not corrected for variation of instrumental sensitivity across the spectrum, with the intensity scale often being arbitrary. Unlike ultra violet visible and infrared absorption spectroscopy, Raman scattering is viewed as a single beam mode, without a reference channel to compensate for instrumental sensitivity variation with time or wavelength[36,37]. Consequently, it is generally difficult to compare relative or absolute Raman intensities from different instruments, and calibration transfer based on intensities is exceedingly difficult. The problem is further compounded by the dependence of observed Raman intensity on focusing and alignment, so that a given sample may yield a significant variation of intensities from day to day, even on a particular instrument and under apparently identical conditions. The main drawback with the use of the Raman spectroscopy as a quantitative technique has been the difficulty in the reliable determination of relative and absolute intensities[36].

Basic theory of peak intensities

The factors that influence the observed Raman intensities can be divided into two categories: sample and laser variables as well as collection and detection variables. Most of these variables are kept constant by using the same spectrometer and laser in addition to checking the Raman signal with a silicon standard.

$$S(e^-) = LA_D\Omega_D TQt \tag{2.17}$$

$$S(e^-) = (P_D \beta DK)(A_D\Omega_D TQt) \tag{2.18}$$

$S(e^-)$ = Observed signal (in photoelectrons), L = Specific intensity, P_D = Laser power density (in photons s^{-1} cm^{-2}), β = Differential Raman cross-section (in cm^2 molecule^{-1} sr^{-1}), D = Number density of scatters (in molecules cm^{-3}), K = Path length (in cm), t = Observation time (in seconds), A_D = Sample area monitored by spectrometer (in cm^2), Ω_D = Collection solid angle of the spectrometer at the sample (in sr), T = Transmission of the spectrometer and collection optics (unitless), Q = Quantum efficiency of the detector (in e^- per photon).

When considering the photometric accuracy in Raman spectroscopy, the most basic issue is the relationship between the observed signal and the sample variables, such as the cross-section and concentration. This basic objective is difficult to achieve because it depends on a large number of variables as shown by equations 2.17 and 2.18. This issue is illustrated by comparing Raman scattering with absorption techniques. For instance the Fourier Transform Infrared spectroscopy (FT-IR), has a reference spectrum that effectively calibrates most of the instrumental variables. Variables such as the detector response, source intensity and optical losses are all relevant to an absorption experiment; however their effects are removed from the final spectrum by calculating a ratio of reference and sample spectra. In Raman spectroscopy however, one usually measures only the scattered intensity with no reference beam. As such the variations in the collection function with time or with wavelength are not compensated for by a reference spectrum[36]. Any such fluctuations are checked for by daily calibration with a silicon standard.

There are three steps that need to be followed to achieve a corrected Raman spectrum that accurately represents the scattering intensity of a given sample as a function of Raman shift[36]:

1. Reproducibility of the observed scattering intensity
2. Correction for variation of instrument response across a Raman spectrum
3. Determination of absolute scattering intensity and absolute Raman cross-sections

The first two objectives can be achieved by more straightforward calibration than the third step, which is more involved. The great majority of applications however, do not require the assessment of absolute intensity, with its accompanying experimental difficulties. Measurements of the cross-section are generally left to the specialists. Reproducible Raman intensities may be achieved with sensible design of sampling optics and reasonable experimental care. Response function correction is not yet routine but it can be applied. The result of the first two steps is a Raman spectrum that accurately reflects relative Raman scattering intensities and is useful for library searching, quantitative analysis and comparison of spectra between libraries[36].

2.4.5. Raman properties of SiC

The salient features of the spectra of Raman SiC polytypes are the appearance of many weaker lines due to the increased number of molecules per unit cell and the decreased symmetry of the crystal forms. There is a splitting of the TO vibration near 794 cm^{-1} into two components TO_1 with a constant frequency and TO_2, which varies with polytype and drops as low as 782 cm^{-1}. The 3C-SiC unit cell has a T_d symmetry yielding one triply degenerate Raman active phonon (T_{2x}, T_{2y}, T_{2z}). This mode is polar and leads to two longitudinal optic (LO) and transverse optic (TO) components. In 3C-SiC, two Raman peaks are therefore observed corresponding to the TO and LO modes at 796 cm^{-1} and 972 cm^{-1}, respectively. The point group for the hexagonal polytypes is C_{6v}. It gives rise to the Raman active A_1, E_1 and E_2 modes. Both E_1 and E_2 are doubly degenerate (E_{1x}, E_{1y} and E_{21}, E_{22}) and only A_1 and E_1 are polar and split in TO and LO phonons[38]. As the unit cell increases, additional phonons with different energies may appear. These new Raman bands are called folded modes, as they correspond to phonon modes located within or at the edge of the Brillouin zone[39].

The intensities of the Raman phonons vary with the orientation of the crystal about the laboratory axes (XYZ). The scattering efficiency (I) is related to the polarization of the incident (e_i) and scattered (e_s) light and is given by $I=C\Sigma_j \cdot |e_i \cdot R(j) \cdot \xi_j \cdot e_s|^2$, where C is a constant, R_j is the Raman tensor and ξ_j is the polarization of the phonon j [40]. The T_2, A_1 and E_1 modes are polar. The intensities of the LO and TO vibrations therefore vary with the propagation directions in the crystal. The intensities of the LO and TO vibrations therefore vary with the propagation directions in the crystal. In the backscattering configuration, the wave vector of the phonon q is parallel to the light propagation. The consequence is straightforward for both the A_1 and E_1 modes: A_1(LO) is active when q is along the c axis of the crystal, whereas the A_1(TO) and E_1(TO) modes are active when q is perpendicular to c. For the cubic zinc-blend crystal, the assessment of the TO and LO peak intensities is more complex. It can be shown, for instance, that the TO mode is strictly forbidden for the (100) crystal orientation, whereas the LO mode is forbidden for the (110) orientation[41].

		Frequency (cm^{-1})			
Polytype	**x = q/q$_B$**	Planar acoustic FTA (E)	Planar optic FTO (E)	Axial acoustic FLA (A_1)	Axial optic FLO (A_1)
3C	0	–	796*	–	972
2H	0	–	799	–	968
	1	264*	764*	–	–
4H	0	–	796	–	964
	2/4	196, 204*	776*	–	–
	4/4	266		610	835
6H	0	–	797	–	965
	2/6	145, 150*	789*	–	–
	4/6	236, 241		504, 514	889
	6/6	266	767	–	–
15R	0	–	797	–	965
	2/5	167, 173*	785*	331, 337	932, 938
	4/5	255, 256	769	569, 577	860
21R	0	–	797	–	967
	2/7	126, 131*	791*	241, 250	
	4/7	217, 220	780	450, 458	905, 908
	6/7	261	767	590, 594	

Table 2.1 – Raman frequencies of fundamental SiC polytypes. The asterisk denotes the Fourier Transverse Acoustic (FTA) and Fourier Transverse Optic (FTO) modes with the maximum intensity in each phonon branch. FLA and FLO are abbreviations for the

Fourier Longitudinal Acoustic and Fourier Longitudinal Optic modes. q/q_B is the reduced wave vector of the corresponding phonon mode SiC[5].

A detailed study of these aspects is made possible by polarization of the Raman scattered light. This property can be measured using (plane) polarized laser excitation and a polarization analyzer. Spectra acquired with the analyzer set at both perpendicular and parallel to the excitation plane can be used to calculate the depolarization ratio. This technique is useful in analyzing the connections between group theory, symmetry, Raman activity and peaks in the corresponding Raman spectra. The spectral information arising from this analysis gives insight into molecular orientation and vibrational symmetry, allowing the user to obtain valuable information relating to the molecular shape. It is often used to understand macromolecular orientation in crystal lattices, liquid crystals or polymer samples[42].

The various Raman frequencies of 3C, 2H, 4H, 6H, 15R and 21R SiC polytypes are given in table 2.1:

From the literature it has been shown that the 973 cm^{-1} photons of the 3C polytype can shift to around 964 cm^{-1}. This effect is attributed to be independent of the excitation radiation, but is more likely due to small crystallites found in the samples. The position, relative intensity and bandwidth of the Raman bands are closely related to the degree of order in the structure and the stress in the material[43].

The Raman bands in SiC crystals containing stacking disorder exhibit broadening and distortion at frequencies corresponding to the basic polytypes (e.g. 4H, 6H, 15R etc.) [44]. For heavily disordered crystals, a broad background is sometimes observed and corresponds to the so-called ‘density of state’ (DOS) contribution, which superimposes between 700 and 1000 cm^{-1}. This phenomenon is as a result of random faulting in the stacking sequence[45]. In disordered SiC, long-range order in the stacking of the atomic layers is lost. The short-range order remains however, comprised of small domains, each consisting of a basic polytype structure. Consequently, the Raman spectra of the disordered structures reflect the structures of the domains[46]. SiC rarely has uniform distribution of the stacking order across the entire crystal. A common feature is that in disordered SiC, disordered zones are sandwiched in between the same or different polytype layers, or are located near the surface region[47,48].

Raman shifts toward high wavenumbers are attributed to macroscopic strain induced during the deposition process and the width is also governed by the lattice imperfection and grain boundaries. Increasing the deposition temperature increases the intensity and lowers the wavenumber. A higher intensity indicates a more perfect crystallinity. A change in the wavenumber is a reflection of the degree of distortion of the crystal lattice and therefore of the residual strain. A lower wavenumber indicates a lower strain[49]. It has also been suggested that a high wavenumber region means that crystals are under external pressure[50].

The FTO to FLO SiC line intensity ratio is thought to be a function of the microscopic composition or the structure of the SiC layer. The variation in the SiC line intensities may be caused by changes in the long-range order of the SiC microstructure. Analysis by the scanning electron microscope has revealed a difference in the surface morphology of the coating with and without a strong LO line. A strong LO line is an indication of large, interlocked grains. If no LO is seen, then a ‘cauliflower’ structure with undefined grains is expected. Furthermore, high deposition temperatures lead to SiC grain size increase, but grain boundary gaps also develop. The structural changes as a result of changes in the coating rate depend on the deposition temperature and the coater size [51].

Silicon and carbon

The amount of silicon which forms in TRISO-coated nuclear particles increases with an increase in the coating rate and a decrease in the deposition temperature. The amount of excess carbon increases with an increase in the deposition temperature and a decrease of the coating rate[51].

Single crystal and polycrystalline silicon are characterized by a sharp Raman line centered at 520 cm^{-1} to amorphous silicon with a broad band extending from 415 to 540 cm^{-1} and centered near 480 cm^{-1} [52].

Diamond gives a strong sharp Raman line at 1330 cm^{-1} [53]. Single crystalline and highly oriented pyrolytic graphite materials show a sharp line at 1580 cm^{-1} [54,55]. The more poorly oriented graphitic materials, e.g. activated carbon or glassy carbon show two broader lines at 1335 to 1340 cm^{-1} and at 1580 to 1590 cm^{-1} [56]. Amorphous carbon yields a broad skewed band extending from 1000 to 1700 cm^{-1} centered near 1500 cm^{-1} [51].

2.5. X-ray powder diffraction

2.5.1. General background

X-Ray Diffraction is a powerful non-destructive technique for the structural analysis of crystalline and polycrystalline phases[57]. It is based on the diffraction of a collimated beam of X-rays by the crystalline planes of a solid phase. X-ray powder diffraction can be applied to determine the SiC polytype distributions. A considerable overlap of individual peaks of the x-ray powder diffraction pattern occurs for the SiC polytypes. The reason for this effect is that polytypes are derived from the same parent structures, but contain different stacking vectors to each other. As a result it is difficult to obtain accurate results from a distribution of the polytypes in a mixture. However, the Rietveld method has been found to be a highly effective approach to solving this problem[58].

X-ray wavelengths are typically in the range of 0.7-2 Å. The XRD spectrum is usually obtained by measuring the diffracted intensity as a function of the diffraction angle 2θ, which is the angle between the incident and diffracted beams and the orientation of the specimen. Different maxima, corresponding to the contribution of the different crystalline planes in the crystal, are obtained when constructive interference of diffracted X- rays occurs according to the Braggs law, $\lambda = 2d\sin\theta$, where λ is the wavelength of the x-rays and d is the inter-atomic planar spacing in the crystal. The technique is extremely sensitive to variations of the inter-atomic planar spacing. In general XRD does not provide spatial resolution, being the measured area of several mm^2. For special applications, spatial resolution approximately 10 μm can be achieved with a microfocus source for films thick enough (1 μm). The penetration depth of the X rays is determined by the absorption length. These characteristics give a strong incentive to also use XRD for the non-destructive analysis of epitaxial films and heterostructures[57].

XRD is also a very useful technique for the analysis of polycrystalline samples. Data related to texture and preferred crystalline orientations, strain, grain size, and crystalline quality of the sample can be obtained from the XRD spectra. For a given orientation of the sample, diffraction will occur from any crystallite with the proper orientation satisfying diffraction conditions. If the crystals are randomly oriented, peaks corresponding to the different planes will appear in the XRD spectrum, and the relative intensity of the different peaks is characteristic of each phase in the material. The amount of preferred orientation can be estimated by comparing the integrated intensities of the different peaks from the calibrated data, once geometrical factors have been corrected. The peak width is also affected by crystalline size and the presence of extended defects in the crystals as dislocations and stacking faults[57]. Determination of accurate compositions in SiC is made difficult because if the significant overlapping of the Bragg reflections from the numerous polytypes as well as texture effects. Results obtained by the traditional quantitative XRD methods are generally unsatisfactory[58].

The diffraction pattern is recorded in digitized form (as a numerical intensity value, y_i) at each of several thousands equal increments, i, in the pattern. The Rietveld method is the same no matter what powder diffraction data are used. The differences among data sources affect the data preparation that is required, whether the steps are in angle or energy, and the instrumental parameters that are refined but not in the method itself. In all cases, the best-fit sought is the best least-squares fit to all of the thousands of y_i ‘s simultaneously. The quantity minimized in the least-squares refinement is the residual, S_y, while the sum is overall data points[59].

$$S_y = \sum_i w_i (y_i - y_{ci})^2 \tag{2.19}$$

Where: $w_i = 1/y_i$; y_i = observed (gross) intensity at the i-th step; y_{ci} = calculated intensity of the i-th step.

There are typically many Bragg reflections contributing to the intensity y_i, observed at any arbitrarily chosen point, i, in the pattern. The calculated intensities y_{ci} are determined from the $|F_K|^2$ values calculated from the structural model by summing the calculated contributions from neighbouring Bragg reflections including the background[59]:

$$y_{ci} = s \sum_K L_K |F_K|^2 \phi(2\theta_i - 2\theta_K) P_K A + y_{bi} \tag{2.20}$$

Where: s = scale factor; K = Miller indices, $h\ k\ l$, for a Bragg reflection; L_K = Lorentz, polarization and multiplicity factors; ϕ = reflection profile function; P_K = preferred orientation function; A = absorption factor; F_K = structure factor for the K-th Bragg reflection and y_{bi} = background intensity of the i-th step.

The least squares minimization procedures result in a set of normal equations that involve derivatives of all the calculated intensities, y_{ci}, with respect to each adjustable parameter. These are soluble by inversion of the normal matrix with elements M_{jk} given by[59]:

$$M_{jk} = -\sum_i 2w_i \left[(y_i - y_{ci}) \frac{\partial^2 y_{ci}}{\partial x_j \partial x_k} - \left(\frac{\partial y_{ci}}{\partial x_j} \right) \left(\frac{\partial y_{ci}}{\partial x_k} \right) \right] \tag{2.21}$$

Where: x_j, x_k = same set of adjustable parameters

This has to do with the creation and inversion of an *m* by *m* matrix, where *m* is the number of parameters being refined. Since the residual function is non-linear, the solution must be found with an iterative procedure in which the shifts, Δx_k, are:

$$\Delta x_k = \sum M_{jk}^{-1} \frac{\partial S_y}{\partial x_k} \tag{2.22}$$

2.5.2. Rietveld method

The presence of multiple phases in powder diffraction patterns leads to degradation of the resolution of the data. For the same counting time, there is a decrease in the intensities of the patterns from the individual components. It has however become evident that with the Rietveld analysis it is possible to obtain accurate estimates of the relative abundances of the component phases[60,61,62,63,64]

Equation 2.23 is the formula for quantitative analysis with the Rietveld method. This method is then similar to the traditional integrated-intensity techniques for phase analysis. The difference is that the advantages obtained from considering the full pattern are retained.

$$W_p = S_p(ZMV)_p \Big/ \sum_{i=1}^{n} S_i(ZMV)_i \tag{2.23}$$

Where: *W* = relative weight fraction of phase *p* in a mixture of *n* phases, S = Rietveld scale factor, Z = number of formula units per unit cell, M = the mass of the formula unit (in atomic mass units), V = the unit cell volume (in Å^3).

The X-ray powder diffraction full-pattern fitting Rietveld method has several advantages[58]:

- It makes use of the full diffraction profile correction factors and hence reduces system effects of preferred orientation, extinction, absorption and instrumental configuration.
- There is more efficient treatment of overlapping peaks resulting in consideration of patterns of great complexity and broader peaks.
- There is correct error propagation for quantitative analysis results, by making use of the standard deviation of the scale factor for each phase (estimation by least squares refinement)
- The sample preparation is relatively easy
- It refines crystal structures and peak profile parameters for individual phases in a mixture, providing interactive adjustments of their properties during the analysis.

Peak intensities

For crystal structures solution and refinement the measured peak intensities must represent a known mapping of the intensity distributions of all the *hkl* reflections onto the 2θ dimension of the powder pattern. The assumptions made during such mapping are that[59]:

I. The sample is composed of randomly oriented crystallites (i.e. no preferential orientation)
II. The crystallites are sufficiently numerous to present just about all possible orientations to the incident beam (i.e. a powder average)

For the *in situ* analysis of intact TRISO coated particles criterion I. is not met because they consist of concentric layers of different phases around a central core. The inner layers are therefore shielded by the outer layers, affecting their diffracted intensities. Since we are however interested in the phases in the SiC layer, we are normalizing to a total phase composition comprising only SiC and Si. This ensures a reliable estimation of the phase ratios in the SiC layer. There are a variety of methods that have been proposed to make sure that such requirements are met, including randomizing sample movements, homogenization with amorphous diluents and crystal size reduction[65].

Micro-absorption

It is required that information about the particle and domain size distribution of each of the phases in the sample be obtained[66,67]. For this reason and because micro-absorption has a small dependence on 2θ, correction for this effect has not yet been implemented in Rietveld analysis. It is possible however to take account of the effects of micro-absorption (and other uncorrected systematic terms) by experimental determination of the constants in the equation 2.23 using a calibration mixture composed of standard materials[64,68,69].

2.5.3. Characterization of SiC by XRD

It has been stated by Ortiz et al,[70] (2001) that quantitative x-ray diffraction is the most suitable method for making accurate measurements of the relative abundance of the SiC polytypes, in order to better understand their processing, microstructural development, mechanical, electrical, electronic and optical properties. Ortiz et al, (2001) used two methods to analyse the 3C, 4H, 6H and 15R polytypes: polymorphic methods and whole pattern methods. The Rietveld method on the other hand is based on analysis of the whole pattern, which is fitted by means of a non-linear least-squares regression. The polymorphic method was found to be easier to operate compared to the Rietveld methods. However it is known that Rietveld methods are more accurate. As was expected, it was found that the Rietveld method gave more accurate results in terms of the quantitative polytype composition analysis of SiC.

Hongchao et al,[58] (1997) studied the quantitative XRD analysis, by the Rietveld method of the 3C, 4H, 6H and 15R polytypes. The detection limit of each polytype was based on the standard deviation. An accurate account of the distribution of the SiC polytypes was obtained. The largest relative error was found to be 13% (for the 4H polytype). However the absolute error was less than 2σ which is why the results were regarded as accurate. When the lower detection limit was 2σ (since the quantitative analysis method can give a more accurate result in this case), the lower detection limit for the above four polytypes, 6H, 4H, 3C and 15R were 1.26, 0.76, 0.78 and 0.82%. Minor high order polytypes were not detectable with the experimental statistics used. Higher order structures tended to form as a result of stacking faults that were introduced into parent structures resulting in main reflections overlapping with those of the parent polytypes.

2.6. High temperature XRD - thermal expansion

2.6.1. Factors influencing cell parameters

There are a number of factors that influence the peak 2θ position as well as the cell parameters. These are[65,71,72]:

- The sample height
- Experimental temperature
- Sample absorption
- Instrumental calibration
- The peak shape model used

2.6.2. Thermal expansion properties of Al_2O_3

The Al_2O_3 thermal expansion data have been determined in the literature by Touloukian et al.[73] and by Taylor[74].

$$c(T) = c_0(1 + c_1 T + c_2 T^2) \tag{2.24}$$

Equation 2.24 is Taylor's expression and was used in conjunction with table 2.2.

	a	c
c_0	4.75814	12.99113
c_1	6.55E-06	6.54E-06
c_2	1.82E-09	2.60E-09

Table 2.2 – The coefficients describing the temperature dependence of the cell parameter of Al_2O_3 using equation 2.24[75]. Units are in Å.

2.6.3. Thermal expansion properties SiC polytypes

The three principal axis coefficients of thermal expansion of 3C, 4H and 6H SiC polytypes are expressed by equations 2.25-2.29 as second-order polynomials along the a-axes and along the c-axes[76,77,78]. It is not reported what fabrication method was used to manufacture the SiC samples but x-ray diffraction was used to collect data.

$$\alpha(3C) = 3.19\times10^{-6} + 3.60\times10^{-9}T - 1.68\times10^{-12}T^2 \tag{2.25}$$

$$\alpha_{11}(4H) = 3.21\times10^{-6} + 3.56\times10^{-9}T - 1.62\times10^{-12}T^2 \tag{2.26}$$

$$\alpha_{11}(6H) = 3.27\times10^{-6} + 3.25\times10^{-9}T - 1.36\times10^{-12}T^2 \tag{2.27}$$

$$\alpha_{33}(4H) = 3.09\times10^{-6} + 2.63\times10^{-9}T - 1.08\times10^{-12}T^2 \tag{2.28}$$

$$\alpha_{33}(6H) = 3.18\times10^{-6} + 2.48\times10^{-9}T - 8.51\times10^{-13}T^2 \tag{2.29}$$

The numerous SiC structural polytypes can be considered to consist of two different types of layer plane stacking sequences, which correspond to the cubic and hexagonal types. The 4H and 6H are structurally similar within their layers (i.e. along the a-axes of those polytypes), and also to within the layer structure of the cubic SiC polytype. It is therefore not surprising that the principal axial thermal coefficients $\alpha(3C)$, $\alpha_{11}(4H)$ and $\alpha_{11}(6H)$ are similar[79]

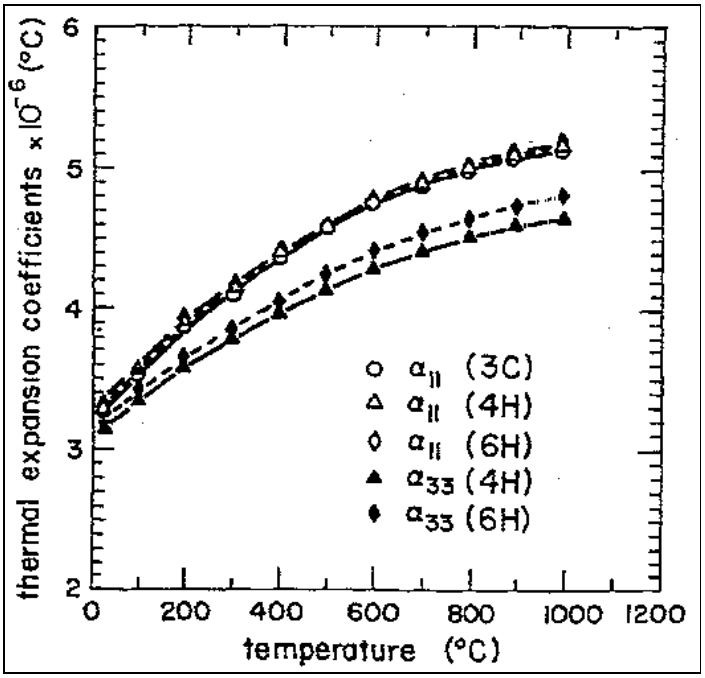

Figure 2.6 – The principal axial coefficients of thermal expansion for the 3C, 4H and 6H SiC polytypes[79].

From figure 2.6 it is evident that the principal axial coefficients of thermal expansion perpendicular to the stacking layers for the 6H and 4H structures are lower than those parallel to, or within the layers. The averages for the three principal axial coefficients of thermal expansion from 20°C to 1000°C can be calculated from the polynomials of equations 2.25-2.27 (along the a-axis) as $\overline{\alpha} = \int \alpha dT / \int dT$, yielding $4.45 \times 10^{-6} /^{o} C$ for $\overline{\alpha}(3C)$, $4.47 \times 10^{-6} /^{o} C$ for $\overline{\alpha}_{11}(4H)$ and $4.46 \times 10^{-6} /^{o} C$ for $\overline{\alpha}_{11}(6H)$. When considering the statistical significance of these averages, the three values are very similar[79].

The averages for the axial coefficients of thermal expansion from 20°C to 1000°C along the c-axis can be calculated from equations 2.28-2.29 to yield values of $4.06 \times 10^{-6} /^{o} C$ for $\overline{\alpha}_{33}(4H)$ and $4.16 \times 10^{-6} /^{o} C$ for $\overline{\alpha}_{33}(6H)$. This confirms that the $\overline{\alpha}_{33}$ values for the 4H and 6H structures are significantly lower than the $\overline{\alpha}_{11}$ values and that the natural decreasing order is $\overline{\alpha}(3C)$, $\overline{\alpha}_{33}(6H)$ then $\overline{\alpha}_{33}(4H)$. This order is the same as that of the density of the H-stacking layers along the c-axes, indicating that the lower thermal expansion coefficients in the <0001> directions for the 4H and 6H polytypes are a direct consequence of the non-cubic stacking layer sequence. Furthermore, it can be deduced that the magnitude of the thermal expansion anisotropy is directly related to the fraction of the H stacking layer sequence in the non-cubic SiC polytypes[79].

The thermal expansion and the thermal expansion anisotropy of crystals depend on two structural factors[80]:

- The strength of the bonds within the structural polyhedra, which directly relate to the nearest-neighbour effects
- The angular changes between the polyhedra or the structural tiltings that relate to the second, third,…,etc., nearest-neighbour effects.

The thermal expansion coefficients of all crystal structures are determined by a combination of these two factors.

The equation for the thermal expansion of polyhedra is derived on a basis related to the strengths of the individual bonds within the crystal polyhedra[81]. This equation expresses the mean linear thermal expansion coefficient between room temperature and 1000°C.

$$\alpha_{1000^o C} = 4.0(4)\frac{N}{S^2 Z_a Z_c}\times 10^{-6} /^o C \qquad (2.30)$$

$\alpha_{1000^o C}$ = mean linear thermal expansion coefficient between room temperature and 1000°C; N = coordination number of the structure; Z_a and Z_c are the cation and anion valencies; S^2 is a factor that is 0.20 for carbides and nitrides.

For SiC the N, Z_a and Z_c are 4. When these values are substituted into equation 2.30, $\alpha_{1000^o C}$ is about $5\times 10^{-6} /^o C$, which is close to the values given by equations 2.25-2.29.

The theoretical coefficient of thermal expansion is only related to the nearest-neighbour atoms and is slightly larger than the reported values. The difference suggests that it is the presence of bond tilting contributions or further removed bonding effects that reduces the overall thermal expansion within the polytypes. The differences from the theoretically calculated coefficient obtained from equation 2.29 are not the same for the a-axis and the c-axis either. It can therefore be concluded that it is the different atom positions in the C and H stacking layer sequences which directly determine the thermal expansion anisotropies of the SiC polytype[79]. There have been other 3C SiC thermal expansion coefficient data reported in the literature. CVD SiC has been analyzed with x-ray diffraction[11] yielding equation 2.31 (units in 10^{-6}/K).

$$\alpha = -1.8276 + 0.0178T - 1.5544E - 05 * T^2 + 4.5246E - 09 * T^3 \qquad (2.31)$$

T(K)	α_L - 3C SiC ($10^{-6}K^{-1}$)	α_L - Graphite ($10^{-6}K^{-1}$)
320	2.93	4.62
340	3.08	4.71
360	3.22	4.80
380	3.36	4.88
400	3.49	4.96
420	3.61	5.03
440	3.72	5.10
460	3.83	5.17
480	3.92	5.23
500	4.01	5.28
520	4.08	5.34
540	4.15	5.38
560	4.21	5.43
580	4.27	5.47
600	4.31	5.50
620	4.34	5.53
640	4.37	5.56
660	4.39	5.58
680	4.40	5.59
700	4.40	5.61
720	4.39	5.61
740	4.39	5.62
760	4.38	5.62
780	4.38	5.61

Table 2.3 – Thermal expansion data of SiC and PyC[82].

Table 2.3 is a set of interferometer-collected data from 3C SiC and PyC of a TRISO particle[82]. The TRISO samples were hollow hemispherical SiC shells, prepared by the fluidized bed method, across a temperature range of 300 K to 800 K.

From a dilatometric study, it has been reported that there exists an inflection point in the 1350°C-1450°C temperature range and hysteresis after a SiC sample has been cycled down through this temperature range when plotting the linear expansion versus temperature as is seen in figure 2.7[83]. The cooling curve does not retrace the heating curve below 1450°C, indicating a change that is not completely reversible. The difference is explained by the slight contraction that free silicon impurity (~1%) experiences when going from the solid to the liquid phase

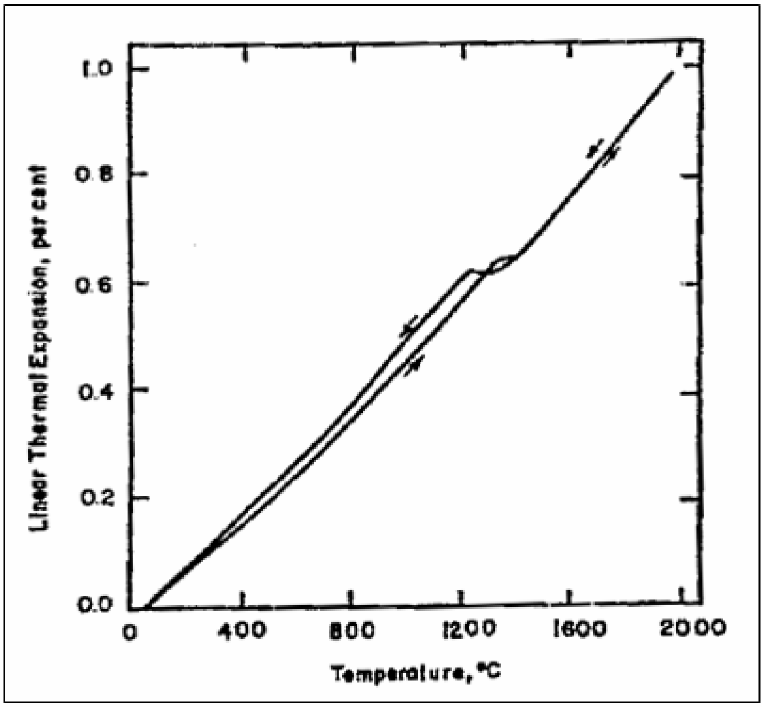

Figure 2.7 – Linear thermal expansion versus temperature relation for β-SiC[83]

2.6.4. The thermal expansion of graphite

It has been shown that the crystal lattice coefficients of thermal expansion parallel and perpendicular to the basal planes may be expressed in the form[84] :

$$\alpha_a = AC_{V_a} + BC_{V_c} + CT$$
$$\alpha_c = LC_{V_a} + MC_{V_c} + NT \qquad (2.32)$$

The two components C_{V_a} and C_{V_c} refer to lattice vibrations parallel and perpendicular to the basal planes respectively.

$$C_{V_a} = 3RD\left(\frac{\Theta_a}{T}\right)$$
$$C_{V_c} = 3RD\left(\frac{\Theta_c}{T}\right) \qquad (2.33)$$

Where, Θ_a and Θ_c = Debye temperatures associated with the lattice vibrations, T = absolute temperature and R = ideal gas constant.

These are expressible by the Debye function:

$$D(x) = \frac{3}{x^3}\int_0^x \frac{z^4 e^z}{(e^z-1)^2}dz \qquad (2.34)$$

Thermal expansion coefficients of graphite have been estimated in the literature. Riley[84], Morgan[85], Kellet and Richards[86] have estimated the coefficients for α_a, as is shown in Table 2.4. These values are compared to those that were experimentally determined by Steward et al.[87].

	$\Theta_a(K)$	$\Theta_c(K)$	A (J/mol)	B (J/mol)	C (deg^{-2})
Morgan	2300	800	1.677E-7	-1.036E-7	-8.30E-11
Kellet and Richards	2280	760	1.777E-7	-1.065E-7	0
Riley	2280	760	1.620E-7	-1.013E-7	0

Table 2.4 – Various coefficients in the expression of α_a[88].

Figure 2.8 shows the plot the α_a curves plotted from table 2.4's coefficients compared with the experimental results of Steward et al.[87]. The non-zero coefficient of the temperature term by Morgan gives a closer solution to the experimental data at high temperatures. Also $\alpha_a = 0$ is predicted to be attained at 393.60^{o}C, which compares well with the 400^{o}C that is found experimentally[88].

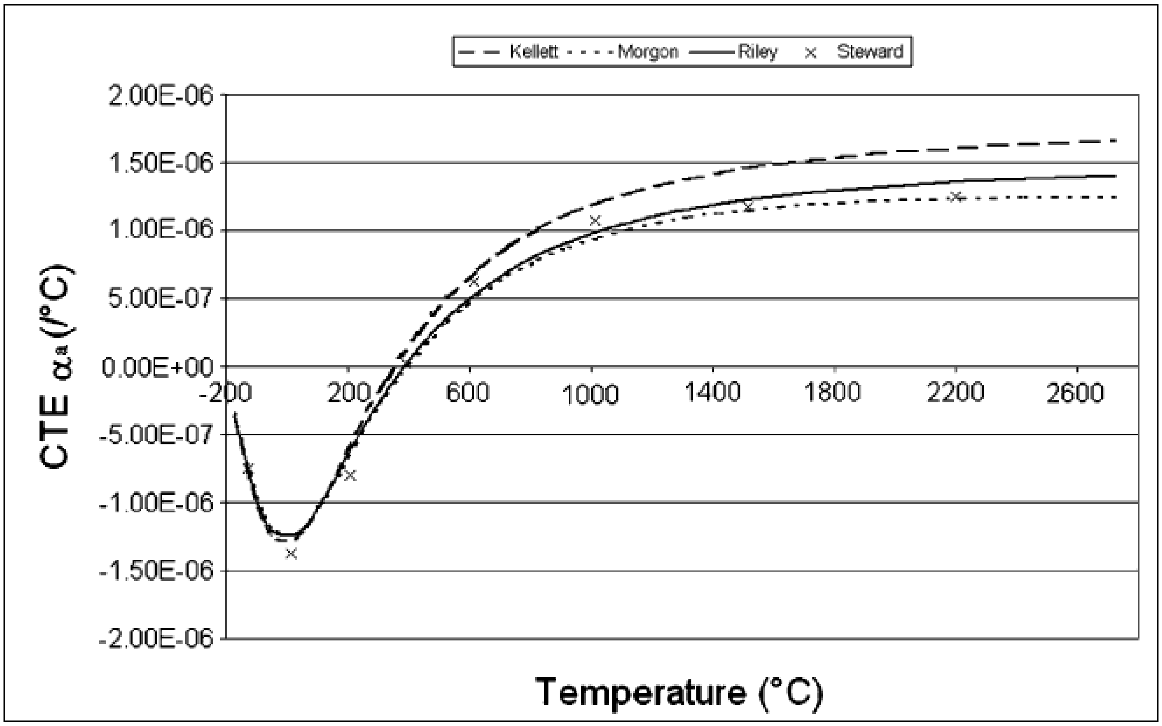

Figure 2.8 – The coefficient of thermal expansion in the a-direction results against temperature[88].

Riley[84] and Morgan[85] have also published their coefficients for the prediction of α_c, with the results shown in table 2.5. The results of Tswang et al.[88], have also been included and better correspond to the experimental values shown in figure 2.9, determined by Steward et al.[87], Nelson and Riley[89], Yates et al.[90] and Harrison[91]. Riley's[84] coefficients give reasonable values at high temperatures but overestimate the α_c at low temperatures.

	$\Theta_a(K)$	$\Theta_c(K)$	L (J/mol)	M (J/mol)	N (deg^{-2})
Morgan	2300	800	-7.93E-7	1.56E-6	7.19E-9
Riley	2280	760	-7.70E-7	1.38E-6	1.08E-8
Tsang et al.	2300	800	-5.05E-7	1.40E-6	5.15E-9

Table 2.5 – Various coefficients in the expression of α_c .

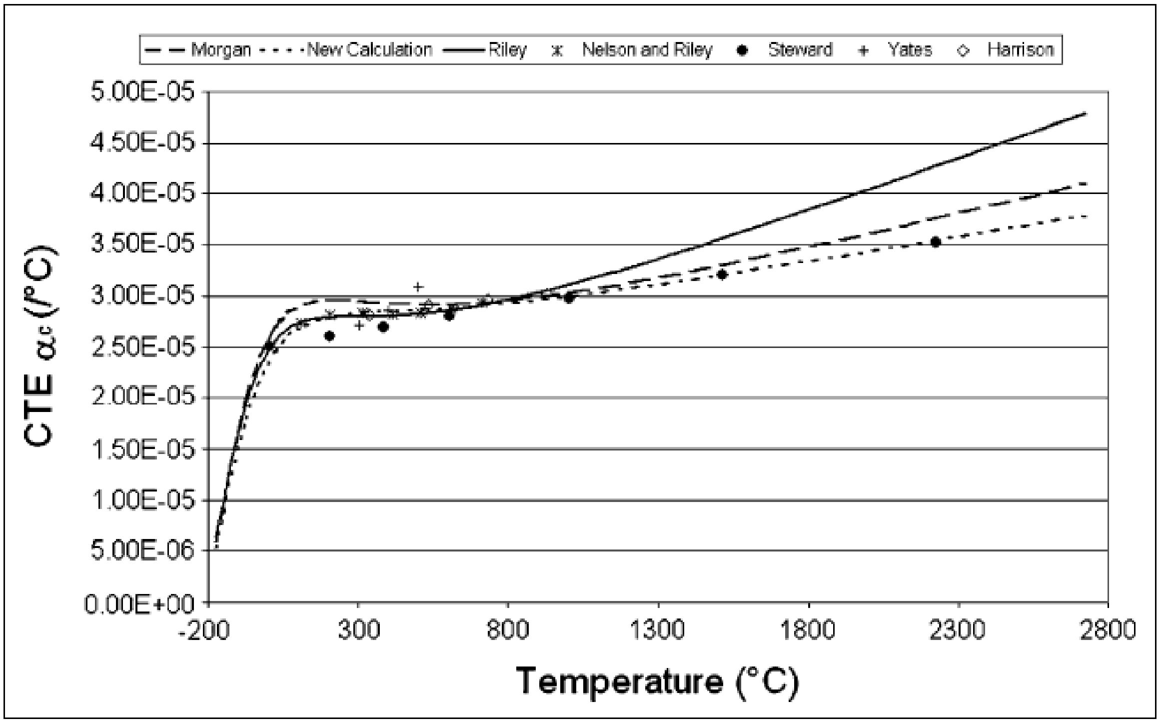

Figure 2.9 – The coefficient of thermal expansion in the c-direction results against temperature[88].

2.7. Transmission electron microscopy

2.7.1. Conventional transmission electron microscopes

In the TEM, a thin specimen is irradiated with an electron beam of uniform current density; the electron energy is in the range 60-150 keV (usually around 100 keV) or 200 keV-3 MeV in the cases of intermediate and high-voltage electron microscopes. Electrons are emitted in the electron gun by thermionic emission from tungsten hairpin cathodes or LaB_6 rods or by field emission from tungsten filaments (used when high gun brightness is needed). The two stage condenser-lens system permits variation of the illumination aperture and the area of the specimen illuminated. A three or four stage lens system images the electron-intensity distribution behind the specimen onto the fluorescent screen. The image is then recorded by direct exposure of a photographic emulsion inside the vacuum or digitally by CCD or TV cameras[92]. The ray diagrams of the TEM are shown in figures 2.10 and 2.11.

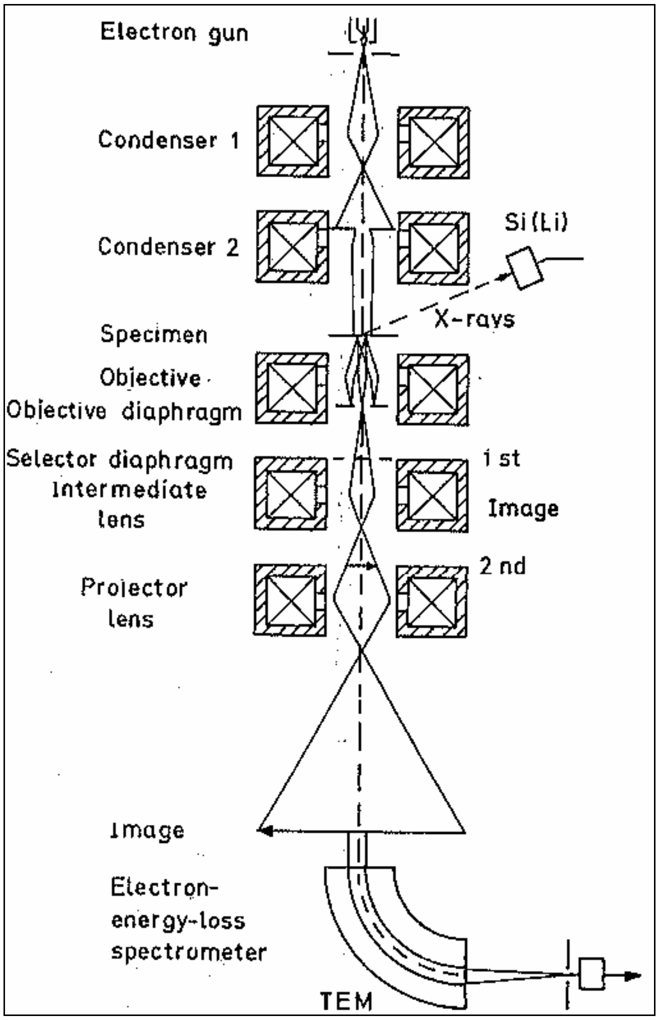

Figure 2.10 – Schematic ray path for a transmission electron microscope equipped for additional x-ray and electron energy-loss spectroscopy[92].

The lens aberrations of the objective lens necessitate the use of very small objective apertures (in the order of 10-25 mrad, to achieve a resolution of 0.2-0.5 nm). The bright field contrast mode is produced by absorption of the electrons scattered through angles larger than the objective aperture (i.e. the scattering contrast) or by interference between the scattered wave and the incident wave at the image point (phase contrast). The phase of the electron waves behind the specimen is modified by wave aberration of the objective lens. The aberration and the energy spread of the electron gun (1-2 eV); limit the contrast transfer of high spatial frequencies. Electrons interact strongly with atoms by elastic and inelastic scattering. This necessitates the use of thin samples of the order 5 nm to 0.5 μm for 100 keV electrons, depending on the density and elemental composition of the object and the resolution desired. Special preparation techniques are used, for instance electropolishing of metal foils. Thicker specimens are investigated with a high-voltage electron microscope. TEM is able to provide high resolution because elastic scattering in an interaction process that is highly localized to the region occupied by the screened coulomb potential of an atomic nucleus. Inelastic scattering is more diffuse and spreads out over about a nanometer[92].

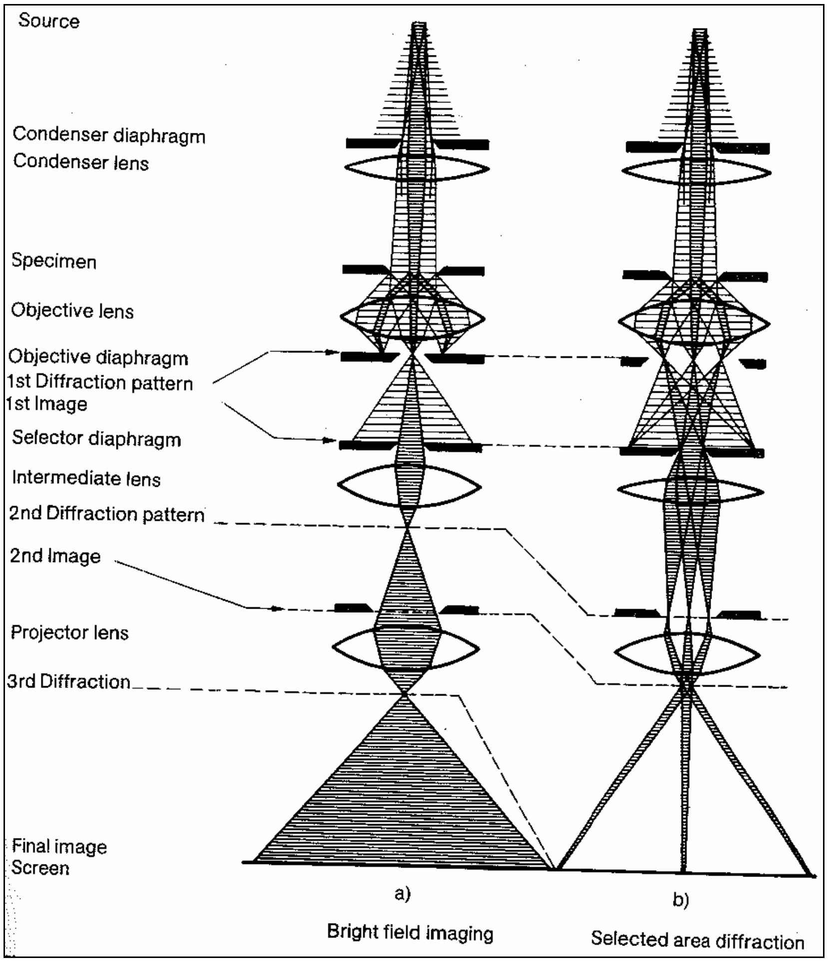

Figure 2.11 – Ray diagram for a transmission electron microscope in (a) the bright field imaging mode and (b) the selected-area electron diffraction mode[92].

2.7.2. Limitations of the TEM

Sampling

As with any high resolution imaging technique, the main limitation is that only a small area can be looked at for any one time. A higher resolution therefore implies worse sampling abilities of the instrument. It is necessary to examine samples with techniques of poorer resolution but better sampling abilities (such as the eye, visible-light microscope and the scanning electron microscope) before utilizing the TEM[93].

Interpreting transmission images

One of the challenges that are associated with the TEM is that it presents us with 2D images of 3D specimens that are viewed in transmission. As a result there are certain artifacts that abound in TEM images. One of the aspects of this drawback is that many of the TEM information such as imaging, diffraction patterns and spectra, is averaged through the thickness of the specimen. Therefore a single TEM image has no depth sensitivity. A full characterization of the specimen would require the assistance of surface sensitive or depth-sensitive techniques[93].

Specimen preparation

It is necessary to have thin samples to get any information from the transmitted electrons of the TEM. A sample is considered thin if it is electron transparent. A prerequisite for a specimen to be transparent to electrons is that it must be thin enough to transmit sufficient electrons such that there is enough intensity falling on the screen or photographic film. This is generally a function of the electron energy and the average atomic number of the specimen. The thinning process does affect the structure and the chemistry of the specimen thereby introducing artifacts[93].

Electron beam damage and safety

Ionizing radiation can damage the specimen particularly in materials such as polymers and some ceramics. The combination of high-kV beams with the intense electron sources that are available means that almost every sample can be destroyed. There is also a danger that is posed to the operator by the ionizing radiation[93].

2.7.3. Electron Diffraction

In the periodic potential of a crystal lattice, the electron waves propagate as a Bloch-wave field, exhibiting the same periodicity as the lattice. The interaction may be characterized by the Bragg condition:

$$\lambda = 2d\sin\theta_B \tag{2.35}$$

This relates the angle 2 θ_B between a Bragg-diffraction spot and the primary beam to the lattice-plane spacing d and the wavelength λ. The kinematical theory of electron diffraction assumes that the amplitude of a Bragg diffracted wave is small compared to that of the primary wave. This is applicable only in for very thin foils which are less than a few nanometers thick. The dynamical theory, which is based on the Schrödinger equation, also describes wave propagation in thick crystals resulting in a 'pendellösung'. This means that the amplitude of the Bragg-diffracted and primary waves oscillate in antiphase as a function of depth and depend sensitively on the tilt of the specimen. The primary beam may show anomalous transmission. A two-beam approximation is often used to discuss the main effects of dynamical electron diffraction on the beam intensity and image contrast in crystals. However, a many-beam theory with 20-100 or more diffracted beams has to be used if the observed phenomena are to be explained in detail. The pendellösung effect causes typical diffraction effects in crystal foils, that can be seen as edge or bend contours. The image intensity depends very sensitively on the strain field of any lattice defects, meaning that a large variety of defects can be imaged and analyzed without resolving the lattice structure. A resolution of the order of 1 nm is attained, if the weak beam technique (in which a dark-field image is formed with a weakly excited Bragg reflection) is used[92].

In the case where the objective aperture is so large that the primary beam and one or more Bragg reflections can pass through the diaphragm, the waves interfere in the image plane forming an interference pattern. This can furnish an image of the crystal structure and its faults, if the specimen is thin enough (≤10nm). The image contrast is often affected by the dynamical diffraction and the phase shift of the electron lens, so that a high resolution image of lattice structures has to be analyzed with care. It is usually necessary to compare the results with computer simulations in which the crystal orientation and thickness and the phase shift caused by the spherical aberration and defocus of the electron lens are considered[92].

2.7.4. The reciprocal lattice

The reciprocal-lattice concept is important for the understanding and interpretation of electron-diffraction patterns[92]. The Laue conditions that govern the occurrence of strong diffraction to occur and are equivalent to the Bragg law are given by equation 2.44[94]:

$$\begin{aligned} \mathbf{P}\,.\,\mathbf{a} &= \mathrm{h}\lambda \\ \mathbf{P}\,.\,\mathbf{b} &= \mathrm{k}\lambda \\ \mathbf{P}\,.\,\mathbf{c} &= \mathrm{l}\lambda \end{aligned} \tag{2.36}$$

The reciprocal lattice (equation 2.45) is derived directly from equations 2.44.

$$\mathbf{P} = h\mathbf{a}^* + k\mathbf{b}^* + l\mathbf{c}^* \tag{2.37}$$

Where, $\mathbf{b}^*$ and $\mathbf{c}^*$ are vectors defined such that $\mathbf{a.a^*} = \mathbf{b.b^*} = \mathbf{c.c^*} = \mathbf{1}$ and $\mathbf{a}^*\,.\,\mathbf{b} = \mathbf{b}^*\,.\mathbf{a}$, etc. = 0. The relations are derived from the fact that $\mathbf{a}^*$ is perpendicular to $\mathbf{b}$ and $\mathbf{c}$ etc. Equation 2.45 is a solution of equations 2.44, since forming the scalar product of equation 2.45 with $\mathbf{a}$ leading to $\mathbf{P}\,.\,\mathbf{a} = \mathrm{h}\lambda$, the first Laue condition. The conditions that $\mathbf{a.a^*} = 1$ and $\mathbf{a.b^*} = 0$ for instance can be explained by the fact that $\mathbf{a}^*$ is perpendicular to $\mathbf{b}$ and $\mathbf{c}$, as is shown in figure 2.12, for non-orthogonal axes.

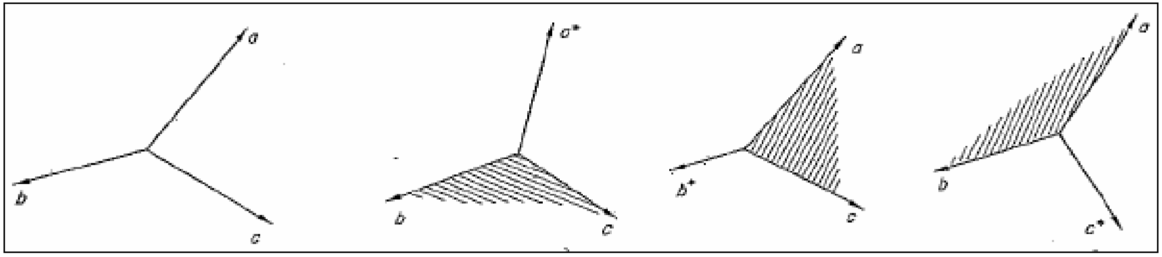

Figure 2.12 – The geometric relationships between the geometric lattice vectors $\mathbf{a}^*, \mathbf{b}^*$ and $\mathbf{c}^*$ and the real lattice vectors a, b, c.

For crystal structures with orthogonal axes (i.e. cubic, tetragonal and orthorhombic), the axes of the reciprocal lattice coincide with those of the crystal lattice[94].

The reciprocal lattice is characterized by two properties:

- The vector $\mathbf{g}_{(hkl)}$ to the point (hkl) of the reciprocal lattice is normal to the plane (hkl) of the crystal lattice
- The magnitude of $\mathbf{g}_{(hkl)}$ is $1/d_{(hkl)}$, where $d_{(hkl)}$ is the interplanar spacing of the family of (hkl) planes

The reciprocal lattice is therefore defined as an array of points, with each of the points corresponding to a particular (hkl) plane as is defined by the two properties above. In figure 2.13, the relationship between planes in the real lattice and point in the reciprocal lattice for a cubic crystal structure is shown[94].

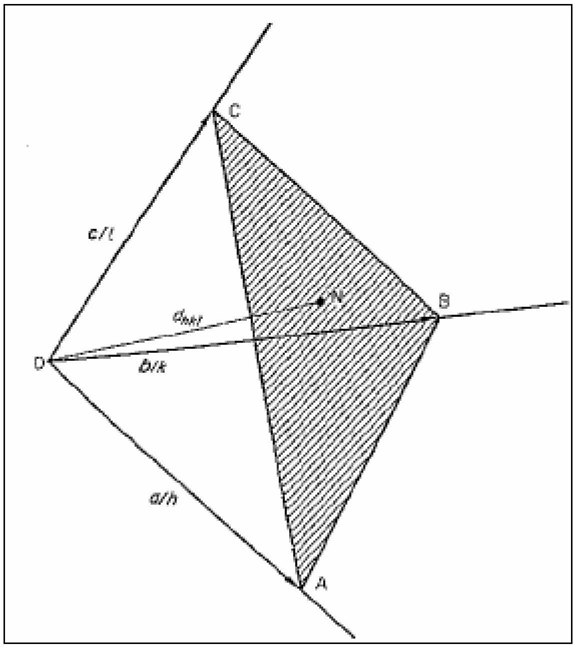

Figure 2.13 – The geometrical relationship between the plane normal and g

3. OBJECTIVES AND HYPOTHESIS

3.1. Objectives and outcomes

The composition and structural integrity of TRISO SiC are important factors in understanding its effectiveness as a barrier to diffusion products. The presence of silicon which melts at 1414^{o}C is particularly detrimental. The transformation of SiC from one polytype to another is known to slightly alter some of the physical and thermal properties. To better understand selected properties of TRISO SiC the following objectives were pursued:

- Phase characterization by means of Raman spectroscopy, XRD and TEM. In addition to the SiC polytypes, the silicon and graphite characterization are critical

- Phase quantification by means of Raman Spectroscopy and XRD

- High temperature stability of SiC up to 1400^{o}C by HT-XRD analysis to provide data for thermal expansion modelling. Of importance is possible phase transformation and volumetric changes

Each experimental technique aids in a unique aspect of characterizing the SiC TRISO layer.

3.2. Hypothesis

The CVD SiC layer properties of the PBMR TRISO coated particle can be characterized in terms of polytypes qualitatively and quantitatively by micro Raman spectroscopy and XRD (Rietveld method). The microstructure can be characterized by TEM.